ESA AO/1-9172/17/I-BG - BALTIC +

BALTIC+ Theme 3
Baltic+ SEAL (Sea Level)

Algorithm Theoretical Baseline Document (ATBD)

From: Technische Universität München
Date: 08.12.2020
To: EUROPEAN SPACE AGENCY (ESA)
Subject: **ESA Contract: 4000126590/19/I/BG - BALTIC+ SEAL (Sea Level)**
Category: ESA Express Procurement Plus –EXPRO+
Deliverable: D3.2
Code: TUM_BSEAL_ATBD

Authors: Felix Müller, Marcello Passaro, Denise Dettmering

Version: 2.1
Reviewed by: Marcello Passaro
DOI: 10.5270/esa.BalticSEAL.ATBDV2.1

Accepted by ESA	Signature	Date
J. Benveniste (ESA-ESRIN)		22/12/2020

LIST OF ACRONYMS

SGDR: Sensor Geopyhsical Data Records

LRM: Low-Resolution-Mode

DD: Delay Doppler

KNN: K-Nearest Neighbour

SWH: Significant Wave Height

OLED: oceanic leading edge detection

PLED: peaky leading edge detection procedure

PP: Pulse Peakiness

MMXO: multi-mission crossover analysis

SSH: Sea Surface Height

VCE: variance component estimation

CONTENT

1. INTRODUCTION

1.1 SCOPE OF THIS DOCUMENT

This document holds the Algorithm Theoretical Basis Document (ATBD) prepared by Baltic+ SEAL team, as part of the activities included in the WP3 and WP4.1 of the Proposal.

The objective of this document is to describe the algorithms used in the development of the sea level dataset for the project.

1.2 STRUCTURE OF THE DOCUMENT

The ATBD is structured as follows:

Section 1 covers the introduction and the description of this document.

Section 2 covers the descriptions of the algorithm used in the classification of the full altimetry dataset

Section 3 presents the algorithms used in the retracking for Low Resolution Mode (LRM) missions and for Delay-Doppler (DD) Altimetry.

Section 4 defines the algorithms used to develop a sea state bias correction.

Section 5 describes the algorithms used in the cross-calibration of the missions.

Section 6 describes the post-processing of the along-track estimations.

Section 7 describes the algorithms employed to produce a gridded dataset.

2 CLASSIFICATION OF FULL ALTIMETRY DATASET

In the winter months, parts of the Baltic Sea (Bay of Bothnia, Gulf of Finland) are covered by a dynamic changing sea-ice layer, which makes continuous, gapless sea-level estimations difficult. Moreover, observations during the winter season are limited to leads (i.e. narrow cracks within the sea-ice) enabling a quick glance on open water. Since these short periodic ocean openings are characterized by very calm water and weak or non-wave movements, the reflected radar signal is much stronger than the one returning from surrounding ice. These strong single peaked radar echoes can dominate registered waveforms, even if the lead is not located at nadir. However, the behaviour of the reflected radar signals is used to classify lead returns and to identify open water areas within the sea-ice layer, which supports a more consistent and gapless determination of sea surface heights in regions affected by sea ice.
The applied open water detection is mainly based on unsupervised, artificial intelligence machine-learning algorithms. The developed algorithm is applicable to all satellite altimetry missions and different radar waveform characteristics. Main input of the classification are recorded waveform and backscatter measurements.
Following section gives an introduction about the open water classification and illuminates the technical background and possible adaptions to the individual satellite altimetry missions. More detailed information can be found in (Müller, Dettmering, Bosch, & Seitz, 2017) .

2.1 INPUT DATA

Main Input of the classification method are altimeter waveforms and information about the backscatter coefficient (σ_0). The coefficient is used to get information about the backscatter characteristics of calm or rough surface conditions. All input data is part of the underlying Sensor and Geophysical Date Records (SGDR). The computation of the backscatter coefficient is dependent on instrumental and dataset characteristics of the particular satellite altimetry missions. In general the computation of σ_0 in decibels is given by following equation:

$$\boldsymbol{\sigma_0 = 10\log_{10}(\max(amp)) + sf + atm_{att}} \qquad \textbf{(2-1)}$$

Where $\mathbf{max}(\boldsymbol{amp})$ gives the maximum amplitude of the waveform in Power Units. $\boldsymbol{sf}$ stands for a scaling factor and $\boldsymbol{atm_{att}}$ the atmospheric attenuation, which are both provided by the SGDR datasets. Some missions (e.g. Envisat, ERS-2, Sentinel-3A/B) need an additional scaling of the waveforms for computing the absolute backscatter coefficient.

However, in case of Sentinel-3A/B the scaling is not well documented and therefore neglected, resulting in relative backscatter values, but displaying the same variability with no impact on the classification results itself.

2.2 DESCRIPTION AND APPLICATION OF UNSUPERVISED CLASSIFICATION STRATEGY

The shape of an altimeter radar waveform, is strongly affected by the reflecting surface (e.g. sea state). Very smooth and flat surfaces (leads, polynyas, calm water) produce single peaked waveforms, whereas more rough surface conditions lead to more noise and multi-peak waveforms (Figure 1). The unsupervised classification algorithm takes advantage of this behaviour and tries to find similarities or patterns among the waveforms related to the specific surface conditions without any pre-known or a priori defined training datasets. This is done by deriving different waveform features (e.g. maximum power, waveform width, slope of the leading edge or noise of the radar echoes) and assigning them to different surface types. The collection of features is also known by the feature space of the classification. Figure 1 shows for Low-Resolution-Mode (LRM) and Delay-Doppler (DD) examples of waveforms with respect to different surface conditions and scatterers. Major variability can be seen in the waveform power, width and noise level.

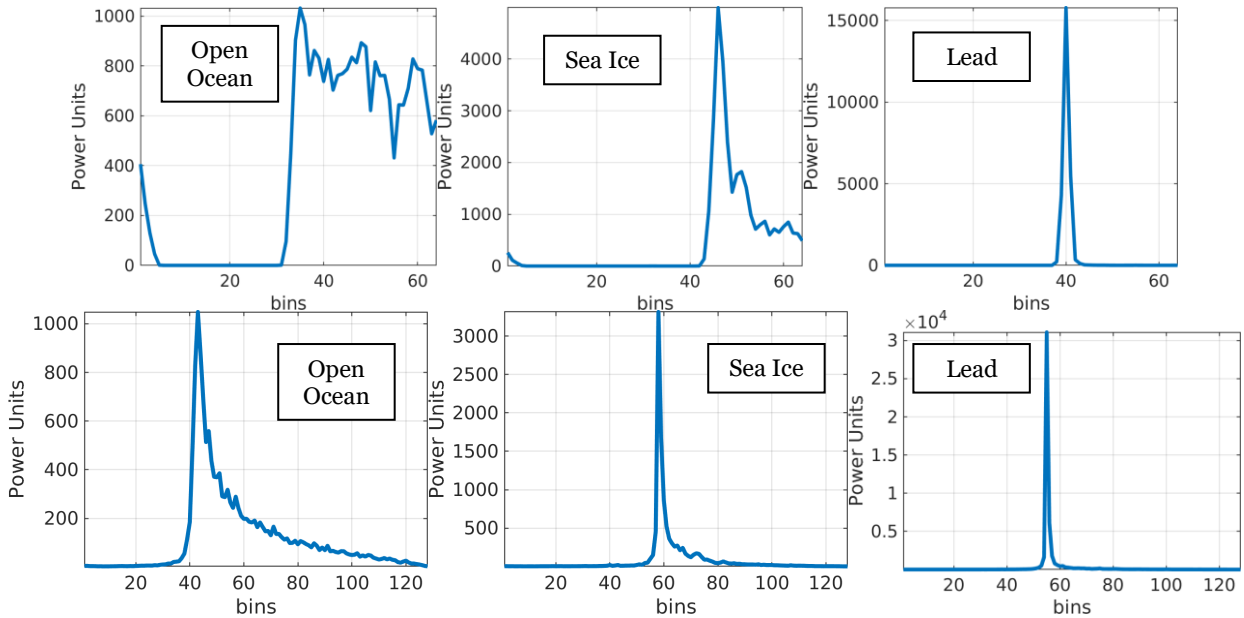

Figure 1: Different waveform example for ERS-2 (LRM altimetry, top row) and Sentinel-3A (DD-SAR Altimetry, bottom row) for three surface conditions

In general, the unsupervised classification is divided into two main steps containing an unsupervised waveform clustering to set up a reference model followed by a classification part to label all remaining waveform data.
At first the reference model has to be created. Therefore, a big set of various radar echoes including preferably all possible surface types is selected. On that account most of the different waveforms are collected during the melting periods to catch various ice types with strong varying backscattering characteristics and shapes.
In order to group the reference datasets automatically into a specific number of clusters representing different waveforms types, the waveforms samples are introduced to a K-medoids clustering algorithm ((Celebi, 2014), (Kaufman & Rousseeuw P., 1990)). In principle K-medoids searches for hidden similarities within the data based on a given input feature space by minimizing the distance (i.e. Euclidean distance) between the individual features and most centrally positioned features (medoids) from the feature space itself. At first the algorithm defines randomly K-medoids followed by the computation of the distance between all features and the initially selected K centres. In the next steps K-medoids rearranges literately the location of the medoids as long as there is no motion among the features. In contrast to the more common known K-means algorithm (Xue & Wunsch, 2009), K-medoids always use centres from the feature space itself, instead of computing averaged centre locations, resulting in more robustness of possible outliers. Since the first medoids are set randomly, which can influence the final clustering result, the algorithm is repeated a couple of times. The cluster run with the final smallest sum of distances, is saved as reference model. K-medoids belongs to the "partitional" clustering algorithms, which require a pre-defined number of clusters K. In the present project K is selected experimentally for DD waveforms and considering previous studies using waveforms of LRM altimetry satellite missions (Müller, Dettmering, Bosch, & Seitz, 2017).
After clustering, the clusters are assigned manually to the different surface types, by using background knowledge about the physical backscattering properties of the individual surface conditions and feature statistic per each cluster. For example, radar waveforms originating from sea-ice show a more diffuse behaviour and a higher noise level than waveforms reflected by calm and more smooth surface conditions. Following bullet points list the used waveform features. The features are applied to all required satellite missions and altimetry datasets. However, slight differences in the computation, due to changed power adjustments, instrumental or specific dataset characteristics are possible. More information, regarding the feature computation can be found in (Müller, Dettmering, Bosch, & Seitz, 2017)

- Waveform maximum - obtained by computation of the physical backscatter coefficient σ_0
- Trailing edge decline - obtained by fitting an exponential function to the trailing edge of the waveform
- Waveform noise – obtained by quantifying trailing edge scattering
- Waveform width – obtained by counting the numbers of bins below a given threshold (e.g. zero)
- Leading edge slope – obtained by subtracting the first bin position containing more than 30% of the power maximum from the bin position of the maximum power. The difference provides relative information about the width and steepness of the leading edge independent of the absolute position of the leading edge, i.e., the range.
- Trailing edge slope – similar to leading edge slope, but number of bins counted from the last bin to first bin from the back exceeding 30% of the maximum waveform power

The second part of the classification is related to the classification of the remaining waveforms. Therefore, K-Nearest Neighbour (KNN) classifier is applied. KNN searches for the closest distance between the reference model and the remaining waveforms (Hastie, Tibshirani, & Friedman, 2009). Please note, in case of KNN, K is defined as the number of K nearest neighbours (waveform clusters of the reference model) of the unknown waveform. The majority of clusters among the K nearest neighbours defines which class has to be assigned to the waveform. In order to evaluate the best number for K, an internal 10-Fold cross-validation is performed (Müller, Dettmering, Bosch, & Seitz, 2017). Parts of the reference model are excluded and re-classified with the remaining model data. The amount of miss-classification gives accuracy information about the reliability of the reference model related to the chosen numbers of K neighbours and the optimal number of neighbours for classifying remaining waveforms. Since the CNES/NASA missions Jason-1, Jason-2 and Jason-3 show similar instrumental, waveform and orbit characteristic as well as ESA/Copernicus DD missions Sentinel-3A and Sentinel-3B only one reference model is developed. In case of the Jason satellites waveform data of Jason-2 and in case of Sentinel-3, Sentinel-3A radar echoes are taken.
Figure 2 shows the 10-Fold cross-validation results for LRM and DD altimetry missions. The classification of CNES/NASA mission Jason-2 and CNES/ISRO mission SARAL/AltiKa display less variability and more stable classification results. Major reasons can be found in a reduced noise level due to a smaller footprint size and improved instrumental characteristics. In case of Delay-Doppler missions the best results are obtained by CryoSat-2. In general, the overall miss-classification rates are small and show a good internal precision of the classification approach. For example, in case of the Jason mission a number of 48 neighbours corresponds to a maximum internal error of about 1.8% and in case of Sentinel-3A/B to 1.2%.

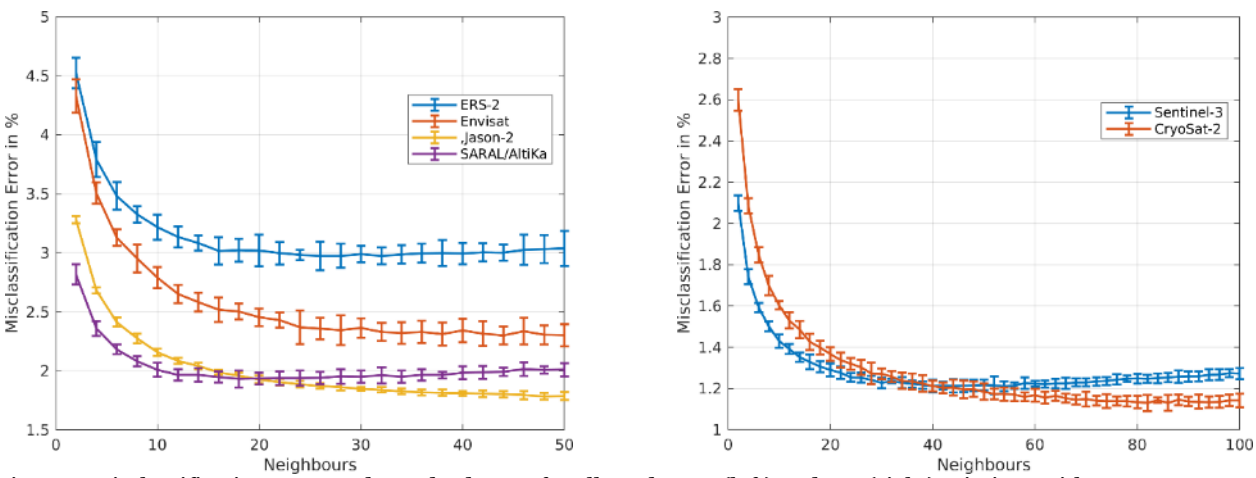

Figure 2 Misclassification error and standard error for all used LRM (left) and DD (right) missions with respect to a varying number of neighbours.

For a better overview Table 1 provides classification information, related to the different missions and waveform datasets. It has to be noted that the open-water detection is based on the same features independent of the mission, however slight adaptions due to different mission specific instrumental and input dataset characteristics are applied. In case of LRM missions more various and noisy waveform shapes are observed, which require a higher segmentation rate of the waveform data into 30 clusters. The higher cluster number enables an easier assessment of the particular waveform clusters to water or non-water conditions. Instead, DD waveforms display a lower noise level and less diffused radar echoes.

Table 1: Used classification parameters and internal accuracy consideration for various altimetry datasets

Mission	Number of clusters	Number of neighbours	Internal miss-classification error
ERS-2 (ESA)	30	24	2.98%(±0.04)
Envisat (ESA)	30	44	2.30%(±0.08)
Jason-1 (CNES/NASA)	30	48	1.79%(±0.03)
Jason-2 (CNES/NASA)	30	48	1.79%(±0.03)
Jason-3 (CNES/NASA)	30	48	1.79%(±0.03)
SARAL/AltiKa (CNES/ISRO)	30	20	1.93%(±0.05)
CryoSat-2 (ESA)	25	80	1.13%(±0.03)
Sentinel-3A (ESA/Copernicus)	25	48	1.20%(±0.02)
Sentinel-3B (ESA/Copernicus)	25	48	1.20%(±0.02)

Also to be noted that since for TOPEX/Poseidon (CNES/NASA) no reliable waveform and backscatter information exists, no unsupervised classification is processed. However, to enable a classification, an external sea-ice concentration of the National Snow and Ice Data Centre (Cavalieri, Parkinson, Gloersen, & Zwally J., 1996) is applied. The fixed threshold between water and sea-ice coverage is set by 25% sea-ice concentration at the individual TOPEX/Poseidon observation locations.

2.3 USAGE OF EXTERNAL AUXILIARY DATA FOR UNSUPERVISED CLASSIFICATION

The classification is performed for all high-frequency along-track waveforms to detect openings within the sea-ice area. However, during clear open ocean conditions for example at the summer time, swell and stronger waves can lead to errors in classification due to a diffuse scattering of the radar signal. Therefore, daily grids of sea-ice concentration, provided by the National Snow and Ice Data Centre (Cavalieri, Parkinson, Gloersen, & Zwally J., 1996), are interpolated to the altimetry high-frequency data to classify safely open ocean conditions. The threshold is set by 0% of sea-ice coverage.
Furthermore, fast ice areas, i.e. sea-ice that is firmly fixed to the shore and does not show any drifting due to currents or wind effects, produce very ocean-like radar reflections. It is not possible to distinguish between real open ocean or fast ice conditions. Hence, external daily sea-ice charts from the Finnish Meteorological Institute (FMI) are applied to identify fast ice areas and flag wrong classified open ocean waveforms. Figure 3 shows an overview on fast ice conditions during April 2016. It can be clearly seen that fast ice only develops close to the coast and in regions with a lot of islands.

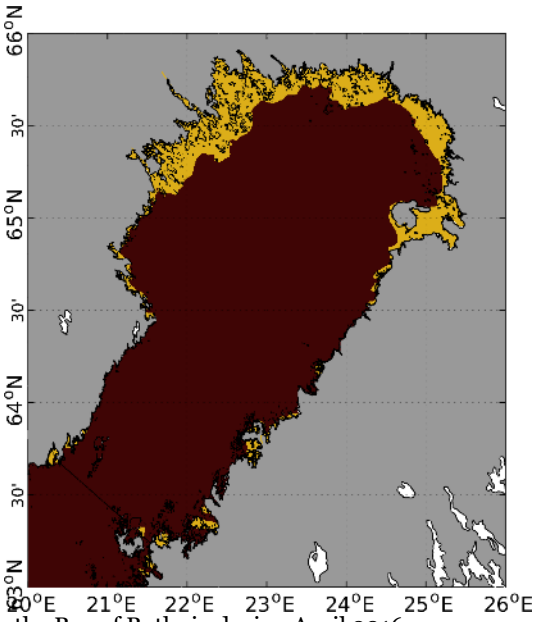

Figure 3: Map of fast ice (yellow) in the Bay of Bothnia during April 2016

The sea-ice charts are nearly complete available for the investigation time and are interpolated to the altimeter locations. In case of missing data, the closest sea-ice chart within ±4 days is used. If no closest sea-ice chart within ±4 days can be found, a mean extent of the fast-area per month is applied to flag the altimeter data by setting up a limit of 50% fast ice coverage at maximum.

2.4 OUTPUT DATA UNSUPERVISED CLASSIFICATION

After applying KNN, the different classes are condensed to water [1] and non-water [0] conditions and can be directly applied as boolean vectors to the individual altimeter tracks. The classification results are saved in NetCDF ("sea_ice_index").

2.5 PROCESSING OF COMPARISON DATA

The classification results are compared to processed SAR and optical images. Therefore, images have to be chosen which are close in space and time to the altimetry overflights to minimize effects of changing surface conditions due to drifting sea-ice. Moreover, optical sensors are affected by clouds and the illumination (polar-night) conditions limiting the availability of suited image data. Table 2 lists the possible comparison pairs considering a maximum acquisition gap of 1 hour and a maximum cloud coverage of 44%. In general, the comparison is spatially limited to January – April and the Bay of Bothnia (i.e. sea-ice season and most northern part of Baltic Sea region)

Table 2 Comparison pairs between altimetry missions and imaging datasets

Altimetry mission	Imaging mission
ERS-2 (E2)	Landsat-5/7
Jason-1, Jason-2, Jason-3 (J1,J2,J3)	Sentinel-1A/B, Landsat-5/7/8, Sentinel-2A/B
CryoSat-2 (CS2)	Sentinel-1A/B, Landsat-7/8, Sentinel-2A/B
Sentinel-3A/B (S3A, S3B)	Landsat-7/8, Sentinel-2A/B

Pairs of imaging and altimetry for Envisat and SARAL/AltiKa are not considered, since their validation was already performed in Müller et al., 2017.

The number and availability of possible comparisons with respect to the validation data is shown in the following plots. It must be noticed that also unusable validation pairs are included. Reasons for missing comparison data can be:

- Very sparse or no spatial overlap within the valid pixel border
- No availability of certain images at the data provider (e.g. offline images)
- No sea-ice area (only open ocean surface conditions)
- Instrumental failure of Landsat-7

The validation covers a theoretical data pool of about 730 Sentinel1-A/B, 450 Sentinel-2A/B and 420 Landsat-5/7/8 snapshots.

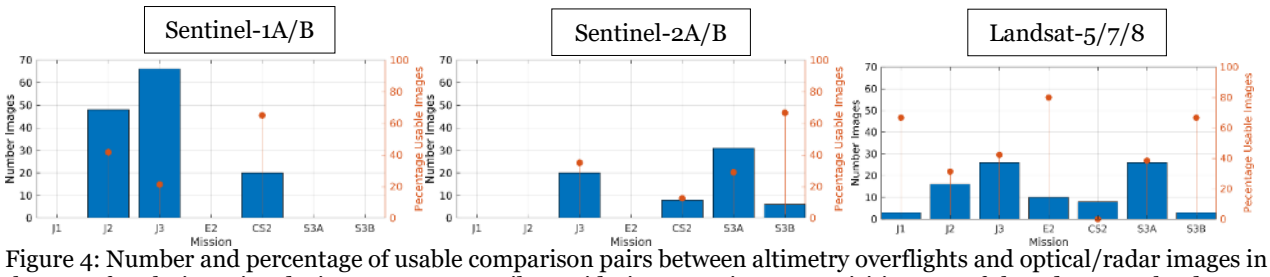

Figure 4: Number and percentage of usable comparison pairs between altimetry overflights and optical/radar images in the Bay of Bothnia region during January – April, considering a maximum acquisition gap of 1h and a max. cloud coverage of 44% in case of optical comparison data.

In case of ERS-2 only a few comparison images are available or can be used. Unfortunately, the repeat cycle times of the Landsat-5/7 and ERS-2 prevent satisfying overlap times and short acquisition gaps. Therefore, a small number of Landsat-5/7 images are used, by also assuming a similar behaviour of the ERS-2 radar altimeter (RA-1) and RA-2 of Envisat. In connection with this issue, it must also be mentioned that radar images of Radarsat-1 show no temporal overlaps within 3 hours.

Optical data processing

Before using the optical images, the spectral bands sensitive for Near Infrared, Red and Green wavelength are selected and combined in order to easily discriminate between land-topography, vegetation, open ocean and sea-ice. The pixel resolution is standardly set by 30m. In case of Sentinel-2A/B pixels are resampled from 10m to 30m spatial resolution being consistent with the Landsat optical data. Figure 5 shows an example of Landsat-8 in April 2016 and Sentinel-2B in March 2019.

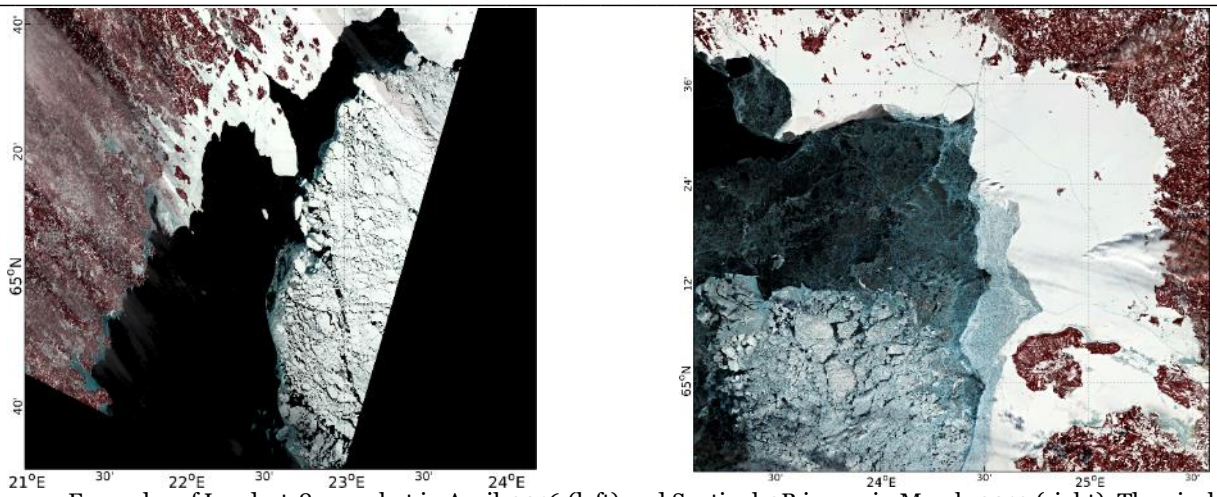

Figure 5 Examples of Landsat-8 snapshot in April-2016 (left) and Sentinel-2B image in March-2019 (right). The pixel resolution is 30m.

Radar/SAR data processing

The radar images of Sentinel-1A/B are processed following the description of Passaro et al., 2017. Briefly summarised, the most important processing steps are:

1. Thermal Noise Removal
2. Speckle-Filtering (Average-Filter)
3. Radiometric Calibration
4. Terrain-Correction

The Sentinel-1A/B images are computed using ESA SNAP Toolbox Version 7.0.3. The toolbox and included sub-programs are following the rules of GNU General Public License. Figure 6 shows a snapshot converted to backscatter values of Sentinel-1B in January 2017. Bright pixels indicate land topography, light grey areas in the image centre are characteristic of the open ocean, while dark regions are typical of very thin ice conditions. The backscatter behaviour is dependent on the surface roughness and conditions.

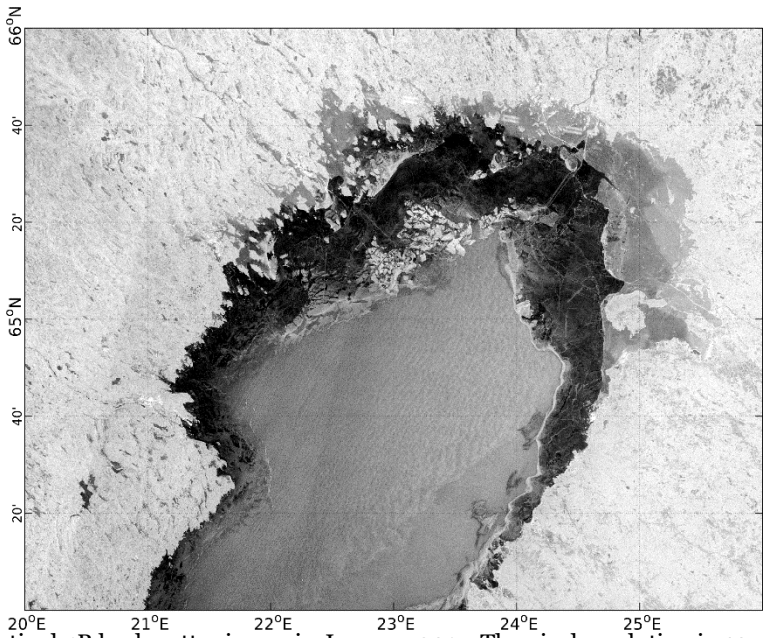

Figure 6 Example of Sentinel-1B backscatter image in January-2017. The pixel resolution is 40m.

2.6 COMPARISON OF CLASSIFICATION WITH OPTICAL AND SAR IMAGES

The comparison results are presented in the Validation Report. The comparison is mainly based on a visual estimation of the reliability of the open-water detection. In general, the unsupervised classification is applicable to all used missions and obtains good classification performances.

3. RETRACKING FOR LRM MISSIONS AND FOR DD ALTIMETRY

3.1 THEORETICAL BACKGROUND: THE BROWN-HAYNE FUNCTIONAL FORM

ALES+ is the retracker that has been further developed and extended to all the missions considered in this project. ALES+ is based on the Brown-Hayne functional form that models the radar returns from the ocean to the satellite. The Brown-Hayne theoretical ocean model [Brown (1977), Hayne (1980)] is the standard model for the open ocean retrackers and describes the average return power of a rough scattering surface (i.e. what we simply call waveform). The return power V_m is modelled as follows (equations reported in Passaro et al., 2014):

$$V_m(t) = a_\xi P_u \frac{|1+\mathrm{erf}(u)|}{2} \exp(-v) + T_n \qquad (1)$$

Where

$a_\xi = exp\left(\frac{-4\,sin^2\,\xi}{\gamma}\right)$ (1b) $\qquad \gamma = sin^2(\theta_0)\frac{1}{2\ln(2)}$ (1c) $\qquad u = \frac{t-\tau-c_\xi\sigma_c^2}{\sqrt{2}\sigma_c}$ (1d)

$v = c_\xi\left(t-\tau-{}^1\!/_2\, c_\xi\sigma_c^2\right)$ (1e) $\qquad \sigma_s = \frac{SWH}{2c}$ (1f) $\qquad \sigma_c^2 = \sigma_p^2+\sigma_s^2$ (1g)

$c_\xi = b_\xi a$ (1h) $\qquad a = \frac{4c}{\gamma h\left(1+\frac{h}{R_e}\right)}$ (1i) $\qquad b_\xi = \cos 2\xi - {}^{sin^2(2\xi)}\!/_\gamma$ (1j)

where c is the speed of light, h the satellite altitude, R_e the Earth radius, ξ the off-nadir mispointing angle, θ_0 the antenna beam width, τ the Epoch with respect to the nominal tracking reference point, σ_c the rise time of the leading edge (depending on a term σ_s linked to SWH and on the width of the radar point target response σ_p), P_u the amplitude of the signal and T_n the thermal noise level.

In practice, the model in equation (1) is a raised sigmoid $\frac{|1+\mathrm{erf}(u)|}{2}$ describing the increasing power in the waveform leading edge and the subsequent plateau, multiplied by a negative exponential which models the reduction of power in the waveform tail (decay), plus thermal (additive) noise T_n. The amplitude of the signal P_u is attenuated by a term a_ξ dependent on mispointing. P_u can be converted into a measurement of the backscatter coefficient σ_0 on the basis of the instrument calibration.

In the case of the DD waveforms, ALES+ adopts a simplified version of the Brown-Hayne functional form as an <u>empirical</u> retracker to track the leading edge of the waveform. While the rising time of the leading edge still has a strict relationship to the significant wave height, the equation 1f does not hold anymore. Moreover, since as explained subsequently a fixed decay of the trailing edge is chosen, the equations 1g-j are not considered. This empirical application of the Brown-Hayne model implies that ALES+ cannot estimate a physical value of SWH and of σ_0. Nevertheless, the retracker is fully able to track the mid-point of the leading edge. To summarise , the simplified version of the Brown-Hayne functional form used to retrack DD waveforms is:

$$V_m(t) = P_u \frac{|1+\mathrm{erf}(u)|}{2} \exp(-v) + T_n \qquad (2)$$

Where

$u = \frac{t-\tau-c_\xi\sigma_c^2}{\sqrt{2}\sigma_c}$ (2a) $\qquad v = c_\xi\left(t-\tau-{}^1\!/_2\, c_\xi\sigma_c^2\right)$ (2b)

Given the experimental characteristic of this approach, which is subject to validation in this project, the range of the original Sentinel-3 A and B product is also provided to the project partners and we keep the option of using the original product if the validation finds the performances of ALES+ to be unsatisfactory for DD retracking.

3.2 LEADING EDGE DETECTION

Since ALES+ is based on the selection of a subwaveform, it is essential that the leading edge, containing the information on the range between satellite and reflecting surface, is correctly detected in all cases. Lead waveforms and ocean/coastal waveforms are characterised in this respect in two different ways: in the first case, the lead return (if at nadir) clearly dominates any other return, but the decay of the trailing edge is extremely quick; in the latter, the leading edge is better characterised, but spurious peaky returns can precede (if from icebergs, ships, or targets at a higher height than the water level) or follow (if from areas of the footprint characterised by different backscatter characteristics) the main leading edge, whose trailing edge decreases very slowly.

LRM waveforms

For the reason above, in ALES+ the leading edge detection for peaky waveforms is different than for oceanic waveforms. To distinguish between the two cases, a Pulse Peakiness (PP) index is computed following the formula in Peacock and Laxon (2004). Waveforms with PP<1 are sent to the oceanic leading edge detection (OLED) procedure, the

others are sent to the peaky leading edge detection procedure (PLED). This is not a physical classification aimed at detecting leads, but only a way to aid the correct detection of the leading edge; moreover, the retracking remains the same in both cases. Peaky waveforms are in our case not only the leads, but any waveform whose trailing edge decay is more pronounced than in the standard ocean return. The aim is therefore different from Peacock and Laxon (2004), in which a strict classification is needed in order to send each kind of waveform to a different retracker and to avoid the detection of false leads, which would determine inconsistencies in the sea level retrieval. Peacock and Laxon (2004) used 1.7 as lead threshold, but in Passaro et al. (2018a) it was already found that the vast majority of waveforms in the area that is not affected by sea ice is characterised by PP<1.
The steps followed by PLED are the following:

1) The waveform is normalised with normalisation factor N, where N = 1.3 * median(waveform)
2) The leading edge starts when the normalised waveform has a rise of 0.01 units compared to the previous gate (startgate)
3) At this point, the leading edge is considered valid if, for at least four gates after startgate, it does not decrease below 0.1 units (10% of the normalised power).
4) The end of the leading edge (stopgate) is fixed at the first gate in which the derivative changes sign (i.e. the signal start decreasing and the trailing edge begins), if the change of sign is kept for the following 3 gates

The steps followed by OLED are the following:

1) The waveform is normalised with normalisation factor N, where N = max(waveform)
2) The stopgate is the maximum value of the normalised waveform
3) Going backwards from stopgate, the startgate is the first gate in which the derivative is lower than 0.001 units

The scope of the normalisation is indeed to take as reference power a value close to the maximum of the leading edge and, in the case of oceanic waveforms with standard trailing edge noise, the proposed factor is a good approximation. Note that OLED would not always work for ocean waveforms (and the same holds for PLED and lead waveforms), since the maximum value may come from spurious reflections and/or noise in the trailing edge.

DD waveforms

For DD waveforms, the OLED threshold is also defined at PP<1 for CS-2, while the threshold for S3a and S3b is set at PP<3. This difference is due to the fact that the current official products of CS-2 and S3 do not follow the same baseline in generating the multilooked waveforms, which result in differences in the typical values of PP in the ocean.

Once this is done, the leading edge is found in a similar way as to LRM, The steps followed by PLED are the following:

1) The waveform is normalised with normalisation factor N, where N = 1.3 * median(waveform)
2) The leading edge starts when the normalised waveform has a rise of 0.01 units compared to the previous gate (startgate)
3) At this point, the leading edge is considered valid if, for at least four gates after startgate, it does not decrease below 0.2 units (20% of the normalised power).
4) The end of the leading edge (stopgate) is fixed at the first gate in which the derivative changes sign (i.e. the signal start decreasing and the trailing edge begins), if the change of sign is kept for the following 3 gates

The steps followed by OLED are the following:

1) The waveform is normalised with normalisation factor N, where N = max(waveform)
2) The stopgate is the maximum value of the normalised waveform
3) Going backwards from stopgate, the startgate is the first gate in which the derivative is lower than 0.01 units

As it can be noticed, the only difference between LRM and DD cases are the checks done during the search of the leading edge. The different values are necessary because of the different signal-to-noise ratio of DD waveforms compared to LRM.

3.3 Choice of Trailing Edge Slope

The choice of the parameters defining the trailing edge slope depends on the kind of altimeter and on the PP of the waveforms. The following cases are found

a) LRM altimeter and standard ocean waveform: In this case, the slope of the trailing edge is defined by the full Brown-Hayne model as already described in 3.1

b) LRM altimeter and non-standard ocean waveform: The non-standard ocean waveforms undergo a further preliminary step: c_ξ is estimated externally. Beforehand, a further check on the PP recomputed on the normalised waveform (Norm PP > 0.3) is computed in order to avoid, where possible, the estimation of c_ξ in the presence of other peaks in the trailing edge. Norm PP is useful because by using a normalised waveform it is easier to set up a threshold for all peaky waveforms regardless of their maximum backscatter power, which greatly differ between specular reflections. The threshold was determined by empirical observation of waveforms. In the external estimation, the full waveform is fitted using the simplified BH model described in (2), having 4 unknowns: τ,σ_c ,P_u, c_ξ. From this result, only c_ξ is kept and used as an input in the remaining steps of the ALES+ algorithm.

c) DD altimeter and standard ocean waveform: here the slope of the trailing edge cannot be physically defined by the full Brown-Hayne functional form. Nevertheless, the trailing edge decay does not influence the fit of the leading edge for a subwaveform retracker such as ALES+, as long as a predefined realistic value is used. In this development phase of ALES+ SAR, the used value is c_ξ=0.04.

d) DD altimeter and non-standard ocean waveform: this procedure follow the same as in b), with the only difference that the further check on Norm PP is not applied, since the higher signal-to-noise ratio of DD waveforms and the fast decay in power after the leading edge makes this check redundant.

3.4 Subwaveform retracking

The ALES+ concept aims at fitting waveforms whose trailing edge is perturbed by areas of the footprint with different backscatter conditions, such as patches of calm waters, land or ice, while guaranteeing a comparable accuracy in typical open ocean conditions.

LRM waveforms

After the preliminary step followed in section 3.4, the retracking for the LRM consists in the following steps:

1. First retracking of a subwaveform restricted to the leading edge, i.e. first estimation of the SWH
2. Extension of the subwaveform using a linear relationship between width of the subwaveform and first estimation of the SWH
3. Second retracking of the extended subwaveform, i.e. precise determination of Range, SWH and sigma0

Defining startgate and stopgate the first and last gate of the subwaveform of choice, in effect the issue is one of defining an appropriate stopgate for a given SWH. The relationship between SWH and stopgate was derived from Montecarlo simulations. For each value of SWH ranging from 0.5 to 10 m in steps of 0.5 m, 500 echoes were simulated with the model in (1) adding realistic Rayleigh noise, and then averaged to create a simulated high-rate waveform. The resulting waveforms were retracked using the classic Brown-Hayne model previously described over the entire waveform, and then over sub-waveform windows with startgate=1 and variable stopgate, and the RMS errors (RMSE) were computed.

Further details on the Montecarlo simulation to derive the stopgate are found in Passaro et al. (2014) and Passaro et al. (2018a). Here we report the relationship used for each reprocessed LRM altimeter in this project.

Envisat: Stopgate = Ceiling (Tracking Point + 2.43 + 4.18*SWH)
Altika: Stopgate = Ceiling (Tracking Point + 2.90 + 3.37*SWH)
Jason1,Jason2,Jason3: Stopgate = Ceiling (Tracking Point + 7.30 + 2.26*SWH)
ERS1, ERS2: Stopgate = Ceiling (Tracking Point +3.17 + 2.32*SWH)

DD waveforms

The use of the Montecarlo simulation as in LRM case is not possible for the empirical application of ALES+ on DD waveforms, since the Brown-Hayne model, even with an adapted c_ξ, cannot be considered as a DD simulator. At the development stage of this project, therefore, the retracking step after 3.4 consists on a single pass on a subwaveform defined as:

Cryosat-2, Sentinel3a, Sentinel3b: Stopgate = Stopgate_{LE} + 20

where Stopgate_{LE} is the last gate of the leading edge.

This agrees with the findings of Thibaut et al. (2014), which showed that also in SAR altimetry a reduced retracking window can be used without significant decrease of the performances. At the current stage of development in this project we are not able to optimise the window according to different levels of σ_c, but the optimization can be an interesting field of improvement if the validation finds that the current strategy guarantees a level of performance similar to the current baseline.

4. SEA STATE BIAS CORRECTION

LRM waveforms

In the standard product, the SSB correction is derived using the methodology described in Gaspar et al. (2002) and Labroue et al. (2004) and updated in Tran et al. (2010). This methodology adopts a non-parametric estimation: a

statistical technique (kernel smoothing) is used to solve a large system of linear equations based on the observations and on a set of weights. The result is a 2D map of the SSB against wind speed and SWH.

20-Hz SSB is the SSB correction derived by using the same 2D map from Tran et al. (2010) and obtained by courtesy of Ngan Tran from Collecte Localisation Satellites, but computed for each high-frequency point using the high-frequency wind speed and SWH estimations from ALES+. The computation of the current SSB model is based on an empirical relationship between three retracked parameters. While part of it is due to the physics of the waves and will manifest itself at low-frequency, the model contains also a relation that is due to the correlated errors in the estimation, which is performed at high-frequency. Applying the SSB model at low-frequency therefore means assuming that the error component of the sea level estimation related to the sea state exists only at long wavelengths, reducing its impact on the short-wavelength components. Further details on the validation of 20-Hz SSB can be found in Passaro et al. (2018b)

DD waveforms

In the original products of DD altimetry, the Sea State Bias correction is either missing (Cryosat-2) or computed using the Jason model. In this study instead, a first model is computed specifically for the ALES+ SAR retracker. As a reference parameter on which the model is built, we take the rising time of the leading edge, which can be used as a proxy for the significant wave height, as shown in figure 7.

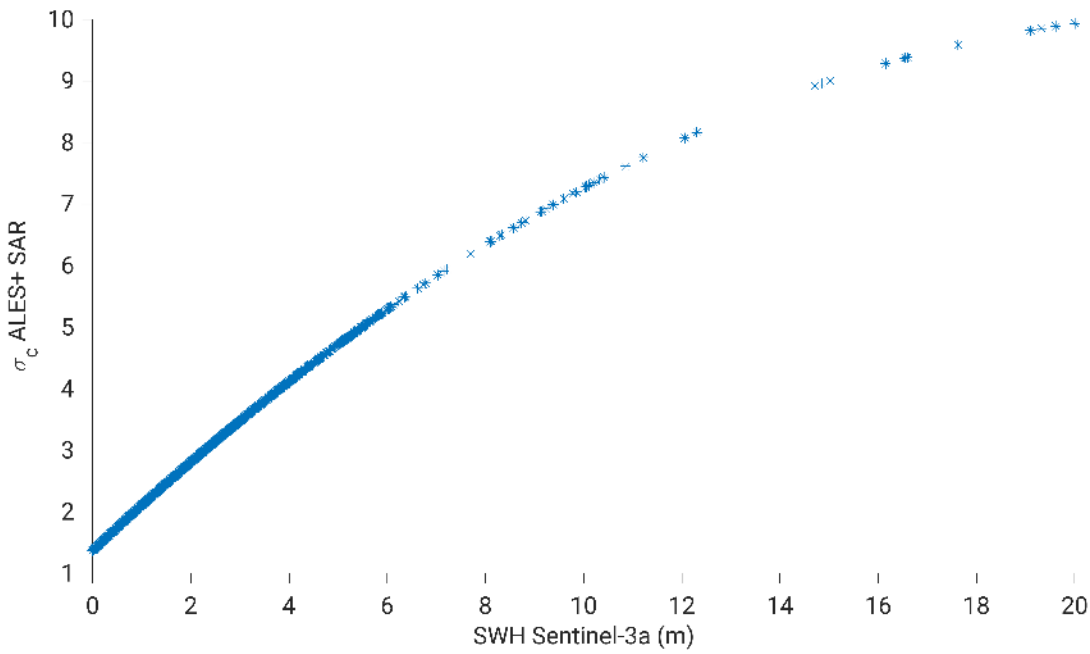

Figure 7: polynomial interpolation of the rising time of the leading edge estimated by ALES+ SAR and the correspondent significant wave height estimated by SAMOSA2 in the original Sentinel-3a product

We derive the corrections by observing the sea level residuals (with no correction applied) at the crossover points. We use a wider region covering the North Sea and the Mediterranean Sea in order to have more open-ocean crossover points, which are scarce in the Baltic Sea. The residuals are modelled w.r.t. the variables influencing the sea state (here the rising time of the leading edge) in a parametric formulation.

$$SSB = \alpha * \sigma_c$$

The equations needed to compute the Sea State Bias model are built using the high-frequency sea level anomalies at each crossover m:

$$\Delta SLA = \alpha\sigma_{c_o} - \alpha\sigma_{c_e} + \varepsilon$$

where o and e stand for odd and even tracks (indicating ascending and descending tracks respectively), ε accounts for residual errors that do not depend on the Sea State Bias correction

We have therefore a set of m linear equations, which we be solved in a least square sense. The chosen α is the one that maximises the variance explained at the crossovers, i.e. the difference between the variance of the crossover difference before and after correcting the sea level anomaly for the sea state bias using the computed model.

In the table below, the variance at the crossover before and after the application of the sea state bias correction is reported, together with the values reported by Gaspar et al., 1994, who estimated the coefficients of Fu-Glazman model (a representation that depends on significant wave height and wind) on a global scale. We also report the results of a high-rate sea state bias correction derived for the standard product of Jason-1 mission in the North Sea by Passaro et al., 2018b. The variance explained by the sea state bias correction in ALES+ SAR is at the same level of the one explained by the high-rate sea state bias correction of Jason-1 and more than the one explained by Gaspar et al., 1994. This is expected, since Passaro et al., 2018b demonstrated that the application of the SSB at high-rate is one way to reduce the intra-1Hz correlation between the retracked parameters. Notably, the crossover variance from ALES+ SAR is lower than in Jason-1, which signals the higher precision of SAR altimetry and of the ALES+ SAR retracking.

Dataset	XO var before SSB (cm^2)	XO var after SSB (cm^2)	Variance explained
Gaspar et al. (1994)	127.7	120.4	6%
SGDR Jason-1 Mediterranean Sea	135.6	108.4	20%
ALES+ SAR Sentinel-3a	106.0	84.9	20%

5. MULTI-MISSION CROSS CALIBRATION

In order to ensure a consistent combination of all different altimetry missions available, a cross-calibration is necessary. We follow the global multi-mission crossover analysis (MMXO) approach described by Bosch et al. (2014) in order to produce a harmonized dataset and a consistent vertical reference for all altimetry missions.
For all crossover locations, a radial correction for both involved observation is estimated by a least squares approach based on SSH crossover differences without the application of any analytic error model. These corrections are later interpolated to all measurement point of all missions included in the analysis. This method was first described by Bosch (2007) as discrete crossover analysis and later applied to different missions, among them Jason-2 (Dettmering and Bosch, 2010) and Saral (Dettmering et al., 2015). Within this approach, the observed crossover SSH differences $\Delta \boldsymbol{x}_{ij}$ are modelled by the difference of two radial error components (of two different passes $\boldsymbol{r}_i$ and $\boldsymbol{r}_j$ at the same time).
Moreover, additional pseudo observations are introduced in order to reduce the differences of consecutive radial errors ($\boldsymbol{r}_i - \boldsymbol{r}_{i+1}$) for one mission:

$$\Delta \boldsymbol{x}_{ij} + \boldsymbol{e}_{ij} = \boldsymbol{r}_i - \boldsymbol{r}_j; \qquad \boldsymbol{0} + \boldsymbol{e}_{i,i+1} = \boldsymbol{r}_i - \boldsymbol{r}_{i+1}$$

Both quantities (the crossover differences as well as the consecutive differences are minimized in a least square adjustment, where $\boldsymbol{e}$ describe the residuals of the problem. In order to account for different uncertainties of the input data, weights are introduced to scale the standard deviation of the crossover differences, the time difference between observations at crossovers, the number of crossovers at different latitudes, and the different mission accuracies. The latter is done automatically by means of a variance component estimation (VCE).
In order to prevent the system from becoming unsolvable, the absolute level of radial errors has to be fixed to solve the rank defect of the system. With other words: only a relative calibration with respect to a reference mission is performed. However, even the mean of radial errors for this reference mission is forced to a fixed value (e.g. originating from an absolute in-situ calibration, set to zero for TOPEX), the single radial errors get non-constant values and may vary geographically and on short time scales.
The basic equation for estimating the radial errors r reads

$$\hat{\mathbf{r}} = (\mathbf{M}'\mathbf{W}\mathbf{M} + \mathbf{k}\mathbf{k}')^{-1}\mathbf{X}'\mathbf{W}_x\Delta$$

where matrix Δ comprises the observed crossover differences, $\mathbf{W}$ and $\mathbf{W}_x$include the weights, $\mathbf{k}$ the constraints and $\mathbf{M}$ and $\mathbf{X}$ are the coefficient matrices. More information on the algorithm can be acquired from Bosch et al., 2014. The approach was developed for global calibration and was adapted for regional applications within this project. This comprises the following points:
(1) The maximum acceptable time difference for the crossover computations has been increased from two days to three days, in order to ensure enough crossover differences in the Baltic sea region.
(2) All crossover points has been used including coastal areas (same reason as 1). To exclude areas impacted by ice coverage, external sea ice concentration information is used.
(3) For the computation of crossover differences, high frequency data are used instead of 1Hz data. This is necessary in order to use retracked ALES ranges. This has been realized by changing the interpolation of along-track heights to crossover locations from point-wise to distance-wise.
(4) All missions are equally weighted. No VCE is performed since the number of observations is too small to generate realistic results. The weighting between crossover differences and consecutive differences has been adapted in order to account for the smaller region.

For all missions used in Baltic SEAL radial errors are estimated. TOPEX MGDR data are used as main reference by setting its mean radial errors per cycle to zero. After TOPEX lifetime, the Jason missions are used as references by fixing their mean bias to constant offsets determined in the overlapping periods with the previous mission. Figure 8 shows the crossover distribution and SSH differences before and after the MMXO for two different cycles (both with four consecutive missions). The table below lists the mean offsets estimated for the different missions in the Baltic Sea (with respect to TOPEX). The small size of the region prevents the generation of geographically correlated error pattern.

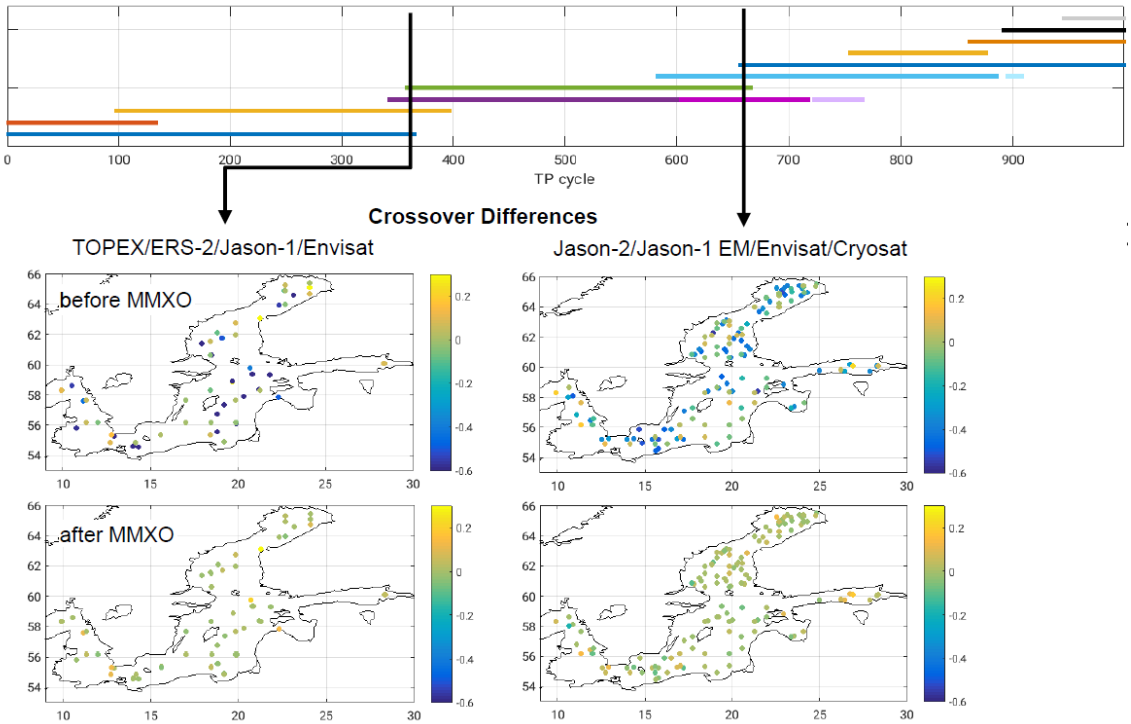

Figure 8: Crossover differences in the Baltic Sea for two 10 day cycles in [m]

Table: Mean radial errors estimated per mission (ALES+ retracker in all cases expect TOPEX and S3A SAMOSA)

Mission	**Mean radial errors [m]**	**Std radial errors [m]**	**No of crossovers #**
TOPEX (MGDR)	0.000	0.037	14834
ERS-2	0.634	0.057	8745
Jason-1	0.125	0.038	22069
Jason-2	0.057	0.039	23986
Jason-3	0.034	0.039	12565
Envisat	0.500	0.071	10687
Cryosat-2 SAR	0.455	0.047	5769
Saral	-0.016	0.044	5641
Sentinel-3A	0.086	0.049	5769
Sentinel-3A SAMOSA	0.035	0.035	4846
Sentinel-3B	0.091	0.050	1795

6. ALONG-TRACK PROCESSING

The sea ice classified observations, the estimated altimeter range, sea state bias, the computed radial orbit differences and atmospheric as well as geophysical corrections are applied to obtain sea surface heights (SSH). Therefore, following altimeter equation is implemented:

$$SSH = H_{orbit} - (R + WT + DT + IONO + SSB + DAC + SET + PT + ROC) \qquad (6.1)$$

where H_{orbit} defines the orbital altitude of the centre of mass of the satellite above the reference ellipsoid (i.e. TOPEX). Further parameters are listed in following Table. Please note, the ocean tide correction is not included to the high-frequent along-track processing, but is added later to the Gridding routines.

Table 1 Altimeter corrections/parameter applied to the along-track processing

Altimeter Correction/ Parameter (short name)	Altimeter Correction/ Parameter (long name)
R	Range
WT	Wet Troposphere
DT	Dry Troposphere
$IONO$	Ionosphere
SSB	Sea State Bias
DAC	Dynamic Atmosphere Corr.
SET	Sold Earth Tide
PT	Pole Tide
ROC	Radial Orbit Corr.

The individual corrections/parameters are explained more in detail in the Dataset Description Table 2 (Ringgaard et. al, 2020)[1].

The corrections are available as along-track data or on a regular grid, which requires a bilinear interpolation to the altimetry track sampling. The unsupervised classification is not directly part of the SSH computation, but is needed to flag altimeter measurements originating from sea ice surfaces. The along-track data is made available without any previous outlier flagging. However, undefined SSH values are possible due to missing corrections or impossible observation conditions. In the following section a strategy of outlier rejection is explained. Possible outliers are indicated in a separate NetCDF entry and can be optionally applied to the SSH retrievals. The described outlier identification follows the chronological order of the implementation. All detected outliers are kept in memory and updated in each outlier detection step for defining a data quality flag (1-0).

6.1 Pre-Gridding Outlier Detection

Pre-defined thresholds, obtained from the along-track dataset itself are applied to the along-track observations, before introducing them to the gridding process. At first true sea ice detected values and observations closer than 3km to the coast are flagged. Further, ranges with re-track fitting errors of >0,3 in case of LRM and >0,1 in case of SAR are labelled as outliers. Furthermore, a Mean Sea Surface (MSS) is interpolated to the observation coordinates and subtracted from the along-track SSH to flag sea level anomalies exceeding ±2m.
In the next two steps the along-track data is flagged in a pass-wise consideration. Therefore, already flagged observations are removed from the dataset. In order to increase the sensitivity of the outlier detection algorithms the along-track SSHs are converted to sea level anomalies.
At first, a running median in connection with a 3-MAD criteria is applied to each track. The median of a 1 second window is checked against the surrounding observations within the window. Elements more than three local MAD from the local median over 1 second are set to outliers.
A second pass-wise outlier detection is referred again to sea ice affected observations and only applied if the sea ice concentration exceeds a threshold of 25% within a 25km grid cell. In order to find unrealistic and erroneous observations, sea ice concentration maps, provided by the National Snow and Ice Data Centre, are interpolated to the altimetry along-track coordinates (Fetterer et al., 2017). Observations within the sea ice domain are defined as outliers, if an element exceeds ±2-MAD of the median of the full pass.

6.2 Gridding and Post-Gridding Outlier Detection

During the gridding process several outlier tests, which are described more in particular in the following section, are performed. Briefly summarized, at first an outlier detection based on a standard 3-sigma criteria followed by an iterative outlier search based on standardized improvements and a T-Test environment is performed.
Beside gridded SSHs, the gridding process returns flagged observations, which are checked, performing a standard Grubbs-Test (e.g. Grubbs 1969) by using already gridded sea level anomalies in the vicinity of the observation.
In a last step the quality flag is the sum of all conducted outlier detection and projected back on the along-track dataset, indicating good (i.e. true) and bad (i.e. bad) observations. Furthermore, the grid flag is saved separately for an optional usage.

7. GRIDDING

Following section explains the generation of monthly grids based on the along-track sea surface height observation, from 1995-05 until 2019-05 (289 months) and a least-squares approach (e.g. Koch, 1999) fitting an inclined plane to the grid nodes.
Please note: Since the ocean tide correction (FES2014) was not applied to the along-track files, it is applied for the gridding process.

[1] Please note changed orbits compared to Dataset Description v1.1 Table2. The updated orbits are listed in the Appendix Table 1.

7.1 Input Data

Current section describes the used altimetry database and the interpolation grid.

7.1.1 Along-Track Altimetry observations

Main input of the gridding process are along-track, in monthly blocks partitioned, SSH observations of the several satellite altimetry missions. Only valid (i.e. true flagged) along-track observations are introduced to the gridding procedure. In order to reach a more mathematically stable least-square estimate, a Mean Sea Surface is subtracted from the along-track SSHs (i.e. sea level anomalies; SLA) reducing the magnitude and value range. In the last step the Mean Sea Surface is re-added to receive SSHs, again.

7.1.2 Unstructured Triangular Grid

The high-frequent along-track altimetry observations are interpolated on an unstructured triangular grid (i. e. geodesic polyhedron). The grid shows a spatial resolution ranging from 6-7 km and covers the entire Baltic Sea.

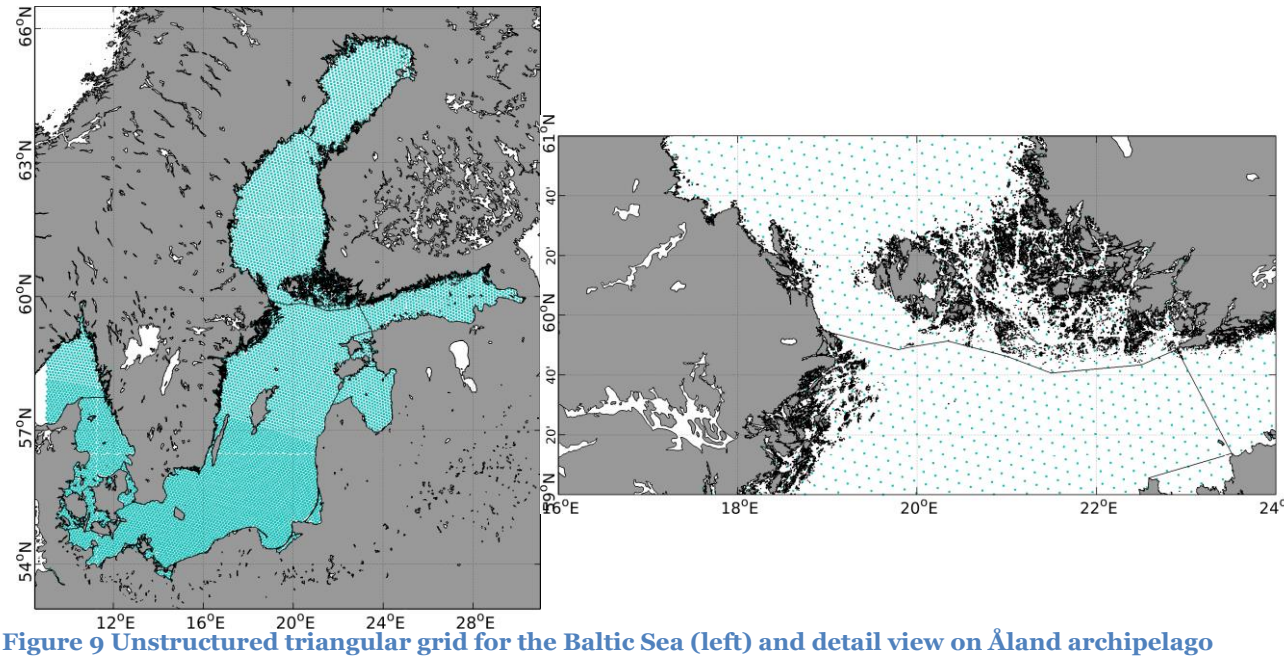

Figure 9 Unstructured triangular grid for the Baltic Sea (left) and detail view on Åland archipelago (right).

7.2 Pre-Processing

Before introducing the altimetry sea surface heights to the gridding procedure, the observation coordinates are converted to a local Cartesian coordinate system (x, y) with the grid node as origin. To include only neighbouring observations, a radius of 100km around the grid node is applied. Only observations within the cap-size are forwarded to a first outlier test, checking the sea level anomalies against a standard 3-sigma criteria. Observations, not fulfilling the criteria are rejected from the further processing, but kept in memory.
In order to get an estimate of the noise and SSH variability of the along-track data, a median absolute deviation of the along-track SSH observation within an area in the open ocean without complex topographic features is computed per mission. The median absolute deviation is used as observation uncertainty information and are placed as variances on the main diagonal of the uncertainty matrix Q_{bb}.
In a next step distance-based Gaussian weights are defined. Therefore, the Euclidean distance between the grid node and the observations are computed. The minimum weight is set to 50% for the most distant observations from the grid node. The Gaussian weights define the weighting matrix W. In a last step the uncertainty information and W are combined to the least-squares weighting matrix P_{bb}, following the equation:

$$P_{bb} = W * \left({}^{1}/_{Qbb}\right) \qquad (7.2.1)$$

7.3 Adjustment of inclined Plane

The gridded SSH are obtained by fitting an inclined plane to each grid node, considering altimetry along-track information within 100km radius around the grid node centre. The mathematical formulation can be written:

$$h(x, y) = c_0 + c_1 x + c_2 y \qquad (7.3.1)$$

The Cartesian coordinates x and y define a tangential plane with the centred grid node. The c-coefficients are estimated using least-squares, c_0 gives the SSH height at the centre grid node, c_1 and c_2 provide information about the slope of the fitted plane, which can be used to compute geostrophic flow.
The unknown c-coefficients are estimated by least-squares following the equations:

$$l + v = A * \beta \ \rightarrow \beta = N^{-1} * A^T P_{bb} l \quad (7.3.2)$$
$$with\ N = (A^T P_{bb} A) \qquad v' P_{bb} v \rightarrow min$$

A, defines the so called Design Matrix and includes all derivatives of the unknowns (c-coefficients). β represents the unknown coefficients and l the observations. v displays the estimated improvement and N stands for the normal equation. The uncertainties of the estimated c-coefficients σ_β, is given by the overall fitting performance σ_0 multiplied with inverse normal equation N. n substitutes the number of measurements and u the number auf unknowns (i.e. 3). T describes transposed matrices.

$$\sigma_0^2 = \frac{v^T P_{bb} v}{n-u} \qquad (7.3.3a)$$

$$\sigma_\beta^2 = \sigma_0^2 N^{-1} \qquad (7.3.3b)$$

Together with the estimated SSH height (i.e. $\beta(1)$), the first element of σ_β includes the standard deviation of the interpolated SSH, which are added to the NetCDF.
In order to eliminate still existing outliers among the along-track data within the cap-size, an iterative outlier search is performed. Therefore, the estimated improvements v are checked against a standard 3-sigma criteria as long as no outliers are detected. Detected outliers are eliminated from the observation vector (l) and the least-squares adjustment is performed, again. Identified outliers are kept in memory.
At a last step an additional outlier rejection based on a Student distribution (e.g. Koch, 1999 & Niemeier, 2008) is performed. Therefore, the standardized improvements (ω) for i-th observation are computed and tested against quantiles of the Student distribution (t), setting the 99th percentile (i.e. $1-\alpha$) as boundary condition. The probability test (P) configuration is described as followed:

$$P\left\{\omega_i = \frac{|v_i|}{\sigma_{v_i}} < t_{n-u,1-\alpha} \mid H_{0_i}\right\} = 1 - \alpha \qquad (7.3.4)$$

The T-Test excludes observations from the least-squares adjustment, if the Zero-Hypothesis H_{0_i} (i.e. $\omega_i > t_{n-u,1-\alpha}$) is rejected. Identified outliers are kept in memory.
σ_v substitutes the standard deviation of the improvements and is computed following the equation:

$$Qvv = Qbb - (AN^{-1}A^T) \qquad (7.3.5)$$
$$\sigma_v^2 = \sigma_0^2 * Q_{vv}$$

The Gridding ends with the output of the SSH, the SSH standard deviation and the number of theoretically and practically usable/used observations per grid node. Furthermore, outliers or rejected observations are transferred to the along-track quality flag processing. However, before they are included to the along-track quality flag, they are checked in a standard Grubbs-Test, using estimated grid nodes in the direct neighbourhood.

7.4 Re-Addition of Mean Sea Surface and Transformation to NetCDF structure

After the gridding process the MSS is re-added to the estimated sea-level anomalies to obtain SSH, again. A threshold of ±2m rejects last unrealistic outliers in the sea-level anomalies, which appeared for example due to a bad observation coverage or difficult environmental conditions (e.g. jagged coastlines, big number of islands).

8. References

Bosch W.: Discrete crossover analysis. In: Tregoning P., Rizos C. (eds.) Dynamic Planet, IAG Symposia 130: 131-136, Springer, 10.1007/978-3-540-49350-1_21, 2007

Bosch W., Dettmering D., Schwatke C.: Multi-mission cross-calibration of satellite altimeters: constructing a long-term data record for global and regional sea level change studies. Remote Sensing 6(3): 2255-2281, 10.3390/rs6032255, 2014

Brown, G, The average impulse response of a rough surface and its applications, IEEE Transactions on Antennas and Propagation, 25, 67-74, 1977

Cavalieri, D., Parkinson, C., Gloersen, P., & Zwally J., H.: Sea Ice Concentrations from Nimbus-7 SMMR and DMSP SSM/I-SSMIS Passive Microwave Data, Version 1. doi:10.5067/8GQ8LZQVL0VL, 1996

Celebi, M. E.: Partitional Clustering Algorithms. Springer International Publishing, 2014

Dettmering D., Bosch W.: Global Calibration of Jason-2 by Multi-Mission Crossover Analysis. Marine Geodesy, 33:S1, 150-161, 10.1080/01490419.2010.487779, 2010

Dettmering D., Schwatke C., Bosch W.: Global calibration of SARAL/AltiKa using multi-mission sea surface height crossovers. Marine Geodesy 38 (supl1): 206-218, 10.1080/01490419.2014.988832, 2015

Fetterer, F., K., Knowles, W., Meier, M., Savoie, and Windnagel.A. K.: Sea Ice Index, Version 3, north, Boulder, Colorado USA. NSIDC: National Snow and Ice Data Center, doi:10.7265/N5K072F8, 2017, accessed 2020-01-15

Gaspar, P., Ogor, F., Le Traon, P.Y. and Zanife, O.Z.: Estimating the sea state bias of the TOPEX and POSEIDON altimeters from crossover differences. Journal of Geophysical Research: Oceans, 99(C12), pp.24981-24994, 1994.

Gaspar, P., Labroue, S., Ogor, F., Lafitte, G., Marchal, L., Rafanel, M.: Improving nonparametric estimates of the sea state bias in radar altimeter measurements of sea level. J. Atmos. Ocean. Technol. 19, 1690–1707, 2002

Grubbs, F. E.: Procedures for Detecting Outlying Observations in Samples, Technometrics: 11, 1-21, doi:10.1080/00401706.1969.10490657, 1969

Hastie, T., Tibshirani, R., & Friedman, J.: The Elements of Statistical Learning (Bd. 2). Springer-Verlag New York. doi:10.1007/978-0-387-84858-7, 2009

Hayne, G. Radar altimeter mean return waveforms from near-normal-incidence ocean surface scattering, IEEE Transactions on Antennas and Propagation, 28, 687-692, 1980

Kaufman, L., & Rousseeuw P., J.: Finding groups in data: an introduction to cluster analysis. New York: Wiley, 1990

Koch, K.: Parameter Estimation and Hypothesis Testing in Linear Models, Springer Berlin Heidelberg, 10.1007/978-3-662-03976-2, 1999

Labroue, S., Gaspar, P., Dorandeu, J., Zanife, O., Mertz, F., Vincent, P., Choquet, D.: Nonparametric estimates of the sea state bias for the Jason-1 radar altimeter. Mar.Geod. 27, 453–481, 2004

Müller, F. L., Dettmering, D., Bosch, W., & Seitz, F.: Monitoring the Arctic Seas: How Satellite Altimetry Can Be Used to Detect Open Water in Sea-Ice Regions. Remote Sensing, 9. doi:10.3390/rs9060551, 2017

Niemeier, W., Ausgleichungsrechnung, De Gruyter, ISBN: 3110190559, URL: http://d-nb.info/986190063, 2008

Passaro M., Cipollini P., Vignudelli S., Quartly G., Snaith H.: ALES: A multi-mission subwaveform retracker for coastal and open ocean altimetry. Remote Sensing of Environment 145, 173-189, 10.1016/j.rse.2014.02.008, 2014

Passaro, M.; Müller, F. L, Dettmering, D., Lead detection using Cryosat-2 delay-doppler processing and Sentinel-1 SAR images, Advances in Space Research, 62, 1610 – 1625, 2017

Passaro M., Rose S.K., Andersen O.B., Boergens E., Calafat F.M., Dettmering D., Benveniste J.: ALES+: Adapting a homogenous ocean retracker for satellite altimetry to sea ice leads, coastal and inland waters. Remote Sensing of Environment, 2018a

Passaro M., Zulfikar Adlan N., Quartly G.D.: Improving the precision of sea level data from satellite altimetry with high-frequency and regional sea state bias corrections. Remote Sensing of Environment, 245-254, 10.1016/j.rse.2018.09.007, 2018b

Peacock, N. R., and Laxon, S. W., Sea surface height determination in the Arctic Ocean from ERS altimetry, J. Geophys. Res., 109, C07001, doi:10.1029/2001JC001026., 2004

Ringgaard, I.M., Madsen, K.S., Müller, F., Tuomi, L.,Rautiainen, L., Passaro, M., Baltic+ SEAL: Dataset Description, Version 1.1. Technical report delivered under the Baltic+ SEAL project. http://doi.org/10.5270/esa.BalticSEAL.DDV1.1., 2020

Rudenko, S., Schöne, T., Esselborn, S. and Neumayer, K. H., GFZ VER13 SLCCI precise orbits of altimetry satellites ERS-1, ERS-2, Envisat, TOPEX/Poseidon, Jason-1, and Jason-2 in the ITRF2014 reference frame, GFZ Data Services, 2018.

Thibaut P., Aublanc J., Moreau T., Boy F., Picot N.: Delay/Doppler waveform processing in the coastal zone. Presented at the 8th Coastal Altimetry Workshop, Lake Constance, Germany, 23-24 October 2014

Tran, N., Labroue, S., Philipps, S., Bronner, E., Picot, N.: Overview and update of the sea state bias corrections for the Jason-2, Jason-1 and TOPEX missions. Mar.Geod. 33, 348–362, 2010

Xue, R., & Wunsch, D. C.: Clustering. Hoboken, N.J. Wiley Piscataway, NJ: IEEE Press Society, I. E. E. E. Computational Intelligence, 2009

APPENDIX

APPENDIX Table 1: Updated Orbits

	Altimeter Missions								
	TOPEX/ Poseidon	Jason-1	Jason-2[2]	Jason-3	ERS-2	Envisat	SARAL/AltiKa	CryoSat-2	Sentinel-3A/B
Orbit	GSFC MGDR-B	GFZ VER13 (Rudenko et. al. 2018)	GSFC std1504_14	CNES GDR-F	Reaper V2 DEOS updated	GFZ VER13 (Rudenko et. al. 2018)	CNES GDR-F	CNES GDR-F	CNES GDR-F

[2] GSFC std1504_14 is not available for the extended mission phase of Jason-2 and substituted by the orbit from SGDR-D files (alt_20hz)